Received 29 November 2020; revised 5 January 2021; accepted 24 January 2021. Date of publication 8 February 2021; date of current version 2 March 2021.

Digital Object Identifier 10.1109/OJAP.2021.3057067

Wideband Printed Half Bow-Tie Antenna Array Based on a Quad-Mode Reconfigurable Feeding Network for UAV Communications

YE-YEONG JEONG (Student Member, IEEE), AND WANG-SANG LEE (Senior Member, IEEE)

Department of Electronic Engineering/Engineering Research Institute, Gyeongsang National University, Jinju 52828, South Korea

CORRESPONDING AUTHOR: W.-S. LEE (e-mail: wsang@gnu.ac.kr)

This work was supported in part by the Ministry of Science and ICT (MSIT), South Korea, through the Institute for Information and Communications Technology Promotion (IITP)—A study on a small antenna system for vehicle supporting wide elevation angle—under Grant 2017-0-00795, and in part by the Korean Government (MSIT) through the National Research Foundation of Korea under Grant NRF-2019R1C1C1008102.

ABSTRACT In this article, a wideband printed half bow-tie antenna array based on a quad-mode reconfigurable feeding network for unmanned aerial vehicle (UAV) communications is presented. The proposed array consists of four printed half bow-tie antennas in the top substrate, two supports with a tapered balun, and a reflector with the reconfigurable feeding network in the bottom substrate. For UAV communications caused by wide beam coverage, the proposed reconfigurable feeding network using one single-pole-four-throw (SP4T) and two single-pole-three-throw (SP3T) switches can adjust the phase and amplitude to the antenna element. By controlling the switches, the proposed array can be operated on four linear polarization modes. The simulated and measured results prove the proposed array reconfigurability of the main beam in four directions with 45° steps in the azimuth plane. In addition, the proposed array achieves the wide 10-dB impedance bandwidth of approximately 29.6% (1507 MHz) from 4.1 to 5.6 GHz. The peak gain and half-power beamwidths (HPBWs) on azimuth and elevation planes of the proposed array are approximately 5.9 dBi, 240°, and 99°, respectively. The overall volume size of the proposed array is $60 \times 60 \times 18.3$ mm^3 ($\sim\lambda_0 \times \lambda_0 \times 0.3\lambda_0$ at 5.1 GHz).

INDEX TERMS Half bow-tie antenna array, low-profile, quad-mode, reconfigurable feeding network, UAV communications.

I. INTRODUCTION

IN RECENT years, the applications of wireless communications have been gradually expanded more than those of wired communications. Similarly, autonomous vehicles, robots, and unmanned aerial vehicles (UAVs) have rapidly been developed and commercialized. Among them, the use of UAVs is rapidly expanding to commercial, scientific, agricultural, and military applications [1], [2]. UAVs can be used in many commercial applications due to their ease of deployment, low maintenance cost, high mobility, and ability to hover [3]. Commercial applications include real-time monitoring and control, providing wireless coverage, remote sensing, search and rescue, delivery of goods, security and surveillance, precision agriculture, and civil infrastructure inspection [4]. Mobile UAVs can establish efficient communication links to deliver messages to ground users, such as sensors [5]. Indeed, they are used routinely to collect and send information back to a base station that provides real-time information on the covered area [6], [7]. Using UAVs as aerial base stations provides several advantages. First, due to their higher altitude, aerial base stations have a higher chance of line-of-sight (LoS) links to ground users. Second, UAVs can easily move and have a flexible deployment, and hence, they can provide rapid, on-demand communications [8], [9]. The data transmission from UAVs is done via wireless links [10]. Therefore, reliable wireless communications are extremely important [11], [12]. Also, UAVs antennas require a small form factor, a low height, and a light weight due to camouflage, efficient power management, and small air resistance [12], [13]. In addition, the polarization mode is also an important factor [14]. In order to avoid discontinuous communications between UAVs and the

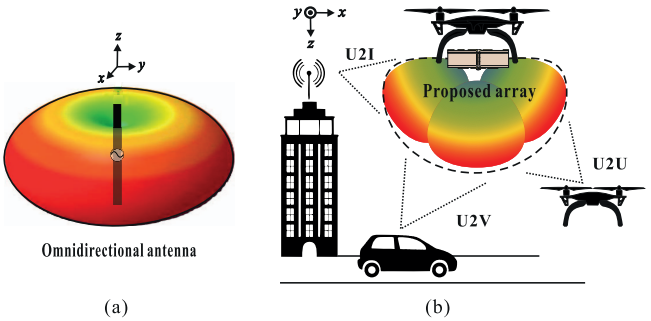

FIGURE 1. Radiation patterns of the typical omnidirectional UAV antenna and the proposed array: (a) the commonly used omnidirectional dipole antenna, (b) the proposed array with the UAV to everything (U2X) communications.

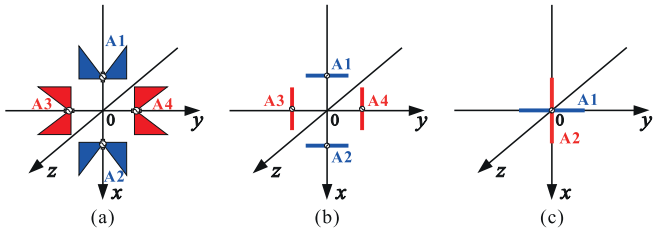

FIGURE 2. Proposed array and simplified models: (a) the top view of the proposed array, (b) two pairs of two-element dipole array, (c) crossed dipole antennas.

base station and to improve communication efficiency, UAVs antennas must have an omnidirectional radiation pattern [15].

The related studies of antennas for UAV applications with an omnidirectional radiation pattern have been conducted [11], [16]–[20]. A lot of compact antennas have been proposed [11], [16]–[18]. Also, [19] and [20] have wider impedance bandwidths than [11], [16]–[18], but both the antenna size and fabrication cost increase. In addition, antennas with these omnidirectional radiation pattern have difficulty transmitting and receiving with the antennas on base stations at different heights. Therefore, UAVs antennas must be able to cover all hemispherical region. Recently, antennas for UAV communications that covers elevation have been proposed [1], [13], [21]–[23]. In [1] and [13], the proposed antennas have a simple structure and small size. However, these designs have drawbacks such as a low gain and narrow impedance bandwidth. Also, a two-element axial-mode antenna array was proposed based on the miniature hexaferrite antenna to further improve antenna gain [21]. The proposed antenna can integrate more functions and decrease in overall size by using a helical structure. In [22], a microstrip antenna with the same size, azimuth, elevation and gain as the antenna proposed in [21] was proposed. The proposed antenna includes a central coaxial-fed disc surrounded by eight tapered strips that are switchable using PIN diodes. Over the operating band 2.35–2.61 GHz, the antenna has a stable gain, and front-to-back ratio of more than 18 dB. Moreover, a dual-band dual-polarized compact bow-tie dipole antenna array was proposed [23]. The proposed antenna array has six horizontal polarizations and six vertical polarizations. However, this array has a large size and numerous states.

Fig. 1(a) shows the typical dipole antenna with an omnidirectional radiation pattern. In the practical UAVs to everything (U2X) communications, UAVs antennas require the hemispheric beam coverage. Fig. 1(b) describes the proposed array with wide-coverage beam patterns in the U2X communications. One of our previous works was a wide beam coverage dipole antenna array with parasitic elements [24]. The proposed array has a wide elevation angle due to the influence of the parasitic element, but there is a limitation to cover the whole hemispherical region due to single beam. Another previous work was a UAV communication antenna array with a 3 × 2 switched beamforming network that forms three beams [25]. The proposed array formed three beams to improve the elevation angle and the gain. Since it was designed to radiate based on the x-axis in the same way as [24], it does not have a sufficient elevation angle for the y-axis. In order to improve the disadvantages of the previous works, we propose a wideband printed half bow-tie UAV antenna array based on a quad-mode reconfigurable feeding network. It generates four linear polarizations with the main beam directions (ϕ) at intervals of 45° for a hemispheric coverage of UAV communications in this article. In addition, the proposed array does not use patch antennas that are difficult to match, such as [11], [22], and [23], and uses bow-tie antennas that are easy to match. In addition, the wide elevation angle and the high gain were achieved by forming multiple beams through a feeding network that adjusts the phase and amplitude by using the linear array antenna theory and crossed dipole antennas analysis.

II. OPERATING PRINCIPLE OF THE PROPOSED ARRAY

In order to understand the operating principle of the proposed printed half bow-tie antenna array with a hemispheric coverage in Fig. 2, the half bow-tie antennas are simplified and replaced with the half-wavelength dipoles. Fig. 2(a) is a top view of the proposed array. As a simplified model of this array, Fig. 2(b) is represented for the analysis. Two pairs of two-element dipole arrays in Fig. 2(b) represent the crossed dipole antennas in Fig. 2(c) using a following analysis based on linear array theory [26].

A. ANALYSIS OF TWO-ELEMENT DIPOLE ARRAY

To understand the principle of operation of four half-wavelength dipoles, it is assumed that the two-element horizontal dipole antenna array positioned along the z-axis of free space. In Fig. 3(a), two antennas are arranged at a distance d interval, and the electric field received at the point P is the sum of the electric fields radiated from the two antennas. The distances from the two antennas to P are r_1 and r_2, respectively. From a far-field condition, $r = r_1 = r_2$ and $\theta = \theta_1 = \theta_2$. The total electric field ($\mathbf{E}$) is:

$$\mathbf{E} = \underbrace{\hat{\phi} E_0 \frac{e^{-jkr}}{r} E_n(\theta, \phi)}_{\mathbf{EF}} \times \underbrace{2\cos\left(\frac{kd\cos\theta + \beta}{2}\right)}_{AF} \quad (1)$$

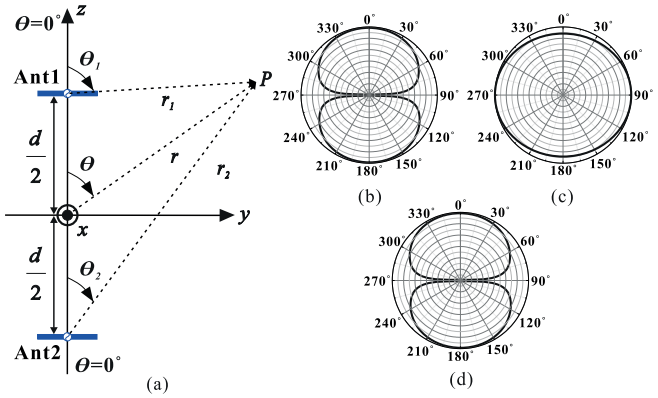

FIGURE 3. Array of two horizontal dipoles positioned along the *z*-axis: (a) the deployment of the array, (b) the radiation pattern of the horizontal dipole antenna, (c) the array factor, (d) the total radiation pattern of the array.

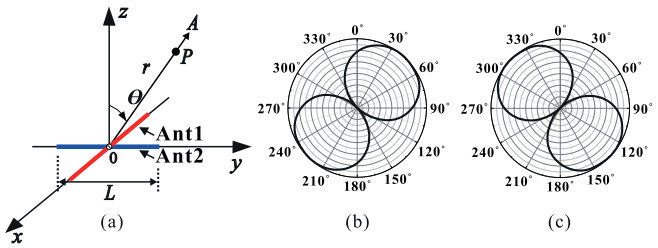

FIGURE 4. Crossed dipole antennas placed on the *xy* plane: (a) the deployment of crossed dipole antennas, (b)–(c) the radiation patterns at β = 0° or 180°.

where E_0, $E_n(\theta, \phi)$, k, β, $\hat{\phi}$, **EF** and AF are the magnitude of the field, the normalized field pattern of a single element ($E_n(\theta, \phi) = \sqrt{1 - \sin^2\theta \sin^2\phi}$), the wavenumber ($2\pi/\lambda_0$) in free space, the phase difference in phase excitation between the two elements, polarization vector of the far-zone E field, the element factor, and the array factor, respectively. Using (1), the expression of the normalized elevation pattern of the array is given by

$$f_n(\theta, \phi) = E_n(\theta, \phi) \times AF_n(\theta, \phi). \tag{2}$$

When the distance d between two horizontal dipole elements is $1/4\lambda_0$ and the β is zero (i.e., same phase excitation of the two-element array), the $E_n(\theta, \phi)$ is zero and the $AF_n(\theta, \phi)$ is approximately 1 on the y-axis ($\theta = 90°$). The total radiation pattern of the array in Fig. 3(d) is obtained by the pattern multiplication between the radiation pattern of the horizontal dipole antenna in Fig. 3(b) and the array factor in Fig. 3(c). Therefore, it has the same radiation pattern as one horizontal dipole antenna located on the y-axis (i.e., the center of two antenna elements).

Likewise, when the two-element vertical dipole antenna array is centered in the y-axis, it can be represented by one vertical dipole antenna positioned along the x-axis.

B. ANALYSIS OF CROSSED DIPOLE ANTENNAS

The proposed array can be seen as crossed dipole antennas placed on the xy plane with the same center at the origin in Fig. 4(a), which the radiation field of the antennas can be calculated by assuming the antenna length (L) of $\lambda/2$ and the same current amplitude with different phase shifts [27]. The radiation fields ($\mathbf{E_1}$ and $\mathbf{E_2}$) of each dipole in a far-field region ($kr \gg 1$, $r \gg \lambda/2\pi$) can be written as

$$\begin{aligned}\mathbf{E_1}(r, \theta, \phi) &= E_{r1}(r)\left[-E_{\theta 1}(\theta, \phi)\hat{\theta} + E_{\phi 1}(\phi)\hat{\phi}\right] \\ \mathbf{E_2}(r, \theta, \phi) &= E_{r2}(r)\left[E_{\theta 2}(\theta, \phi)\hat{\theta} + E_{\phi 2}(\phi)\hat{\phi}\right]\end{aligned} \tag{3}$$

where

$$\begin{aligned}E_{r1}(r) &= E_0 \cdot \frac{e^{-jkr}}{r}, \quad E_{r2}(r) = E_0 e^{j\beta} \cdot \frac{e^{-jkr}}{r}, \\ E_{\theta 1}(\theta, \phi) &= \frac{\cos\left(\frac{\pi}{2}\sqrt{1 - \cos^2\theta \cos^2\phi}\right)}{\cos\phi \cos\theta}, \\ E_{\theta 2}(\theta, \phi) &= \frac{\cos\left(\frac{\pi}{2}\sqrt{1 - \cos^2\theta \sin^2\phi}\right)}{\sin\phi \cos\theta}, \\ E_{\phi 1}(\phi) &= \frac{\cos\left(\frac{\pi}{2}\cos\phi\right)}{\sin\phi}, \quad E_{\phi 2} = \frac{\cos\left(\frac{\pi}{2}\sin\phi\right)}{\cos\phi}.\end{aligned} \tag{4}$$

According to the input phase difference ($\beta = 0°$ or $180°$) between the antennas (1 and 2), the $E_{r2}(r)$ becomes $\pm E_{r1}(r)$. Therefore, the total radiation field ($\mathbf{E_T}$) of crossed dipole antennas with different phase shifts can be obtained by

$$\begin{aligned}\mathbf{E_T}(r, \theta, \phi) &= \mathbf{E_1}(r, \theta, \phi) + \mathbf{E_2}(r, \theta, \phi) \\ &= E_{r1}(r)\begin{bmatrix}(-E_{\theta 1}(\theta, \phi) \pm E_{\theta 2}(\theta, \phi))\hat{\theta} \\ +\left(E_{\phi 1}(\phi) \pm E_{\phi 2}(\phi)\right)\hat{\phi}\end{bmatrix}.\end{aligned} \tag{5}$$

From (5), the axial ratio (AR) using the ratio of orthogonal components of the $\mathbf{E_T}$ can be written as

$$\mathrm{AR} = \frac{|E_\theta(\theta, \phi)|}{|E_\phi(\phi)|} = \left|\frac{-E_{\theta 1}(\theta, \phi) \pm E_{\theta 2}(\theta, \phi)}{E_{\phi 1}(\phi) \pm E_{\phi 2}(\phi)}\right|. \tag{6}$$

The radiation field of the crossed dipole antennas at $\theta = \pi/2$ (i.e., the xy plane) can be expressed as

$$\mathbf{E_T}(r, \theta, \phi) = E_{r1}(r)\left[E_{\phi 1}(\phi) \pm E_{\phi 2}(\phi)\right]\hat{\phi}. \tag{7}$$

In this case, since the AR = 0, these antennas has the linear polarization (LP). Using (7), the azimuth radiation pattern of the crossed dipole antennas placed on the xy plane ($\theta = \pi/2$) can be obtained by

$$|\mathbf{E_T}(r, \theta, \phi)| = \left|E_{r1}(r)\left[E_{\phi 1}(\phi) \pm E_{\phi 2}(\phi)\right]\right|. \tag{8}$$

Figs. 4(b) and 4(c) show the azimuth radiation patterns of the crossed dipole antennas with regard to the $\beta = 0°$ or $180°$, respectively.

C. HALF BOW-TIE ANTENNA ARRAY

The half-wavelength dipole as an element of an array antenna decreases the beam elevation angle. Moreover, the dipole antenna array cannot obtain a wide bandwidth due to a single resonance caused by the antenna length. For several wireless communications services and control of UAVs, the proposed antenna element utilizes a wideband antenna with a bow-tie shape. By adjusting the angle of inclination in the bow-tie

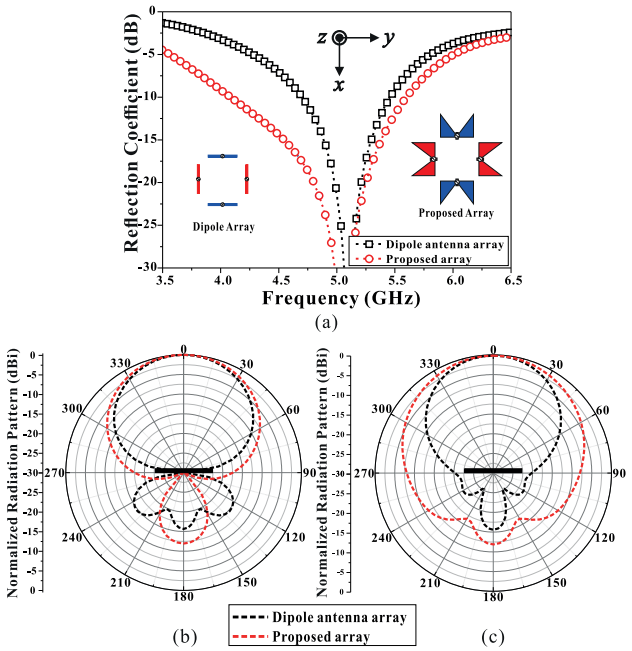

FIGURE 5. Characteristic comparison between the dipole antenna array and the proposed half bow-tie antenna array: (a) the simulated reflection coefficients, (b)–(c) the simulated radiation patterns of a two-element array or two pairs of an orthogonally deployed two-element array at the main beam directions ($\phi = 0°, 45°$), respectively.

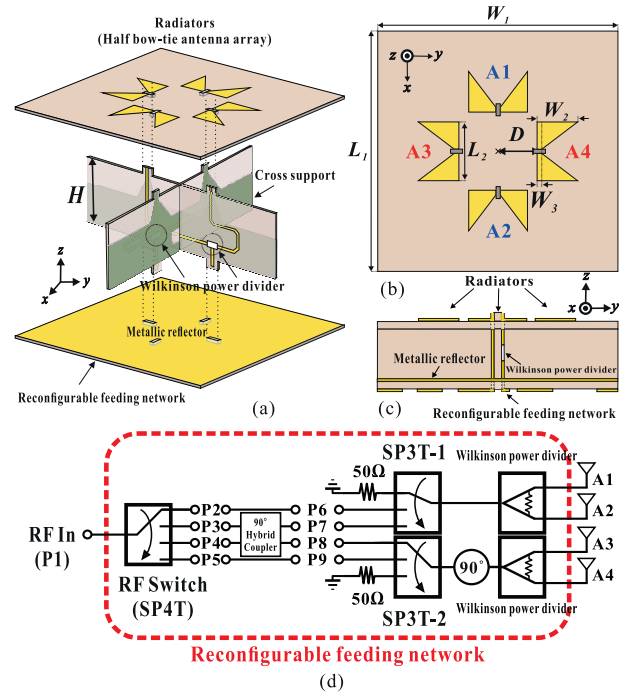

FIGURE 6. Overall configuration of the proposed array: (a) a perspective view, (b) a top view of the radiator with four half bow-tie antennas, (c) a side view, (d) a block diagram of the proposed reconfigurable feeding network.

antenna, the input impedance can be adjusted. Increasing the angle of the antenna allows the reactance of the input impedance to be kept to a minimum over a wider bandwidth. In particularly, the real part of the input impedance is less

TABLE 1. Each distribution of amplitudes and phase variations with regard to the input modes.

Distributions		Mode 1	Mode 2	Mode 3	Mode 4
SP4T States		P2	P3	P4	P5
Output (Ampl., Phase)	A1	$1/\sqrt{2}$, 0°	1/2, 0°	1/2, 0°	-
	A2	$1/\sqrt{2}$, 0°	1/2, 0°	1/2, 0°	-
	A3	-	1/2, 180°	1/2, 0°	$1/\sqrt{2}$, 0°
	A4	-	1/2, 180°	1/2, 0°	$1/\sqrt{2}$, 0°
SP3T-1 or SP3T-2 States		P6 / 50 Ω	P7 / P8	P7 / P8	50 Ω / P9
Beam Direction (ϕ)		0°	135°	45°	90°

susceptible to the operating frequency variation. Therefore, the broadband effect can be obtained in the bow-tie antenna. The reason why a half bow-tie antenna instead of bow-tie antenna is used is to reduce the port coupling between the orthogonal polarizations. In addition, by using a half bow-tie antenna, a uniform beam can be formed and the resonant frequency band can be shifted to the lower frequency band. Fig. 5(a) shows the simulated reflection coefficients of the dipole antenna array and the proposed half bow-tie antenna array with four antenna elements. Their 10-dB impedance bandwidths are 752 MHz and 1590 MHz, respectively. The bandwidth of the proposed array is improved over the dipole antenna array. Figs. 5(b) and 5(c) show the simulated radiation patterns of a two-element array or two pairs of an orthogonally deployed two-element array. The beamwidth of the proposed array is wider than that of the dipole antenna array.

III. PROPOSED ARRAY CONFIGURATION AND ITS DESIGN

A. OVERALL CONFIGURATION OF THE PROPOSED ARRAY

Fig. 6 represents the overall configuration of the proposed array. All substrates of the proposed array use TACONIC RF-60 ($\varepsilon_r = 6.15$, and $\tan\delta = 0.002$). Their thicknesses are 0.64 mm and the copper thicknesses are 18 μm. Fig. 6(a) describes the overall configuration of the proposed array with the proposed reconfigurable feeding network for quad-mode polarizations. The antenna design parameters in Fig. 6(b) are $L_1 = W_1 = 60$ mm, $L_2 = 14.6$ mm, $W_2 = 9$ mm, $W_3 = 1$ mm, $D = 9.8$ mm, and $H = 18.3$ mm. The proposed array consists of antenna radiators (four half bow-tie antenna array) in the top substrate, two supports with four tapered baluns, and a metallic reflector with the reconfigurable feeding network in the bottom substrate in Fig. 6(c). The metallic reflector has an important role of reducing back radiation and enhancing the radiation gain while it is a ground plane of the proposed feeding network for the quad-mode antenna feeding. Fig. 6(d) shows the block diagram of the proposed reconfigurable feeding network.

The proposed reconfigurable feeding network consists of one single-pole quadruple-throw (SP4T) switch, one 90° hybrid coupler, two single-pole triple-throw (SP3T) switches, a 90° delay transmission line, and two Wilkinson power

TABLE 2. Comparison between previous works for UAV communications and the proposed array.

Comp.	f_c (GHz)	HPBWs			Bandwidth (%)	Size ($\lambda_0 \times \lambda_0 \times \lambda_0$)	Gain (dBi)	Antenna type
		Azimuth	Elevation					
[1]	0.9	360°	180°	180°	0.7	0.1 × 0.1 × 0.7	2.6	Folded printed quadrifilar helix antenna
[11]	0.8 / 1.4 / 2.4	360°	–	–	0.5 / 1 / 1.3	0.3 × 0.2 × 0.1	1.5 / 3 / 4	Tapered patch
[13]	0.8	360°	197°	–	3.41	0.1 × 0.4 × 0.03	1	L-shaped monopole
[17]	2.4	360°	–	–	2.1	0.8 × 0.8 × 0.03	2.6	SIW-Multihorn
[18]	2.7	360°	–	–	2.6	1.4 × 1.4 × 0.03	2.5	Slot antenna
[19]	0.7	360°	–	–	6.46	0.4 × 0.4 × 0.02	1.9	HMCPA
[20]	1 / 2.1	360°	–	–	4.2 / 56.1	2.5 × 2.5 × 1	0.9 / 3.9	Square segmented loop
[21]	8	360°	–	–	180	6 × 6 × 0.9	-0.68 to 5.5	Tapered cavity-backed flushmountable antenna
[23]	2.4	-	60°	60°	3.7	1.4 × 1.4 × 0.1	4.5	Hexaferrite helical antenna
[24]	2.4	240°	60°	60°	10.8	1.4 × 1.4 × 0.1	4.5	Micro.Patch
[25]	2.4 / 5	240°	60°	60°	3.5 / 14	2.5 × 2.5 × 1	4.5 / 5	Micro.Patch
Prop.	**5.1**	**240°**	**98.6°**	**98.6°**	**29.6**	**1 × 1 × 0.3**	**5.9**	**Half bow-tie antenna array**

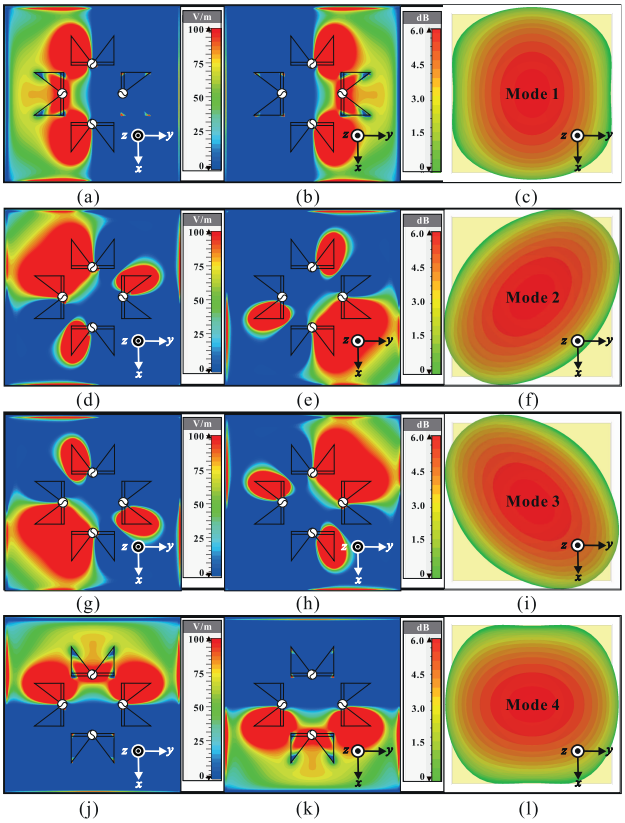

FIGURE 7. Electric field distributions and 3D radiation patterns with regard to input modes: (a)–(b) electric field distributions when the signal phase $\phi = 0°$ or $180°$ in Mode 1, (c) 3D radiation pattern in Mode 1, (d)–(e) electric field distributions when the $\phi = 0°$ or $180°$ and $\beta = 180°$ in Mode 2, (f) 3D radiation pattern in Mode 2, (g)–(h) electric field distributions when the $\phi = 0°$ or $180°$ and $\beta = 0°$ in Mode 3, (i) 3D radiation pattern in Mode 3, (j)–(k) electric field distributions when the $\phi = 0°$ or $180°$ in Mode 4, (c) 3D radiation pattern in Mode 4.

dividers. Using the feeding network, four LPs are obtained by controlling the RF switches. The input switches of the four polarization modes are denoted by P2–P5. The output ports of the feeding network are denoted by A1–A4. Table 1 shows each distribution of amplitudes and phase variations with regard to the input modes. These modes are selected by using the SP4T switch when the RF input signal is applied. When the signal of the modes (Mode 1 or Mode 4) is fed to P2 (or P5), the signal is directly connected to P6 (or P9). After the signal passes through the Wilkinson power divider, it is fed to A1 and A2 (or A3 and A4). Each antenna of these modes has a half power with a same phase. The polarization formed at these modes achieves a linear polarization with a 0° (or 90°) tilted angle. When the signal of the modes (Mode 2 or Mode 3) is fed to P3 (or P4), P7 and P8 are selected and all four antennas (A1–A4) radiate. In this case, each antenna has a quarter power and the phase difference between the A1 and the A3 or the A2 and the A4 is 180° (or 0°). The polarization formed at these modes achieves a linear polarization with a 135° (or 45°) tilted angle. As a result, by switching the input modes, the quad linear polarization are achieved.

B. POLARIZATION CONTROL USING THE PROPOSED FEEDING NETWORK

Fig. 7 shows the electric field distributions and three-dimensional (3D) radiation patterns with regard to input modes (Mode 1–Mode 4). Figs. 7(a)–(b) or 7(j)–(k) show the electric field distributions when the signal phase $\phi = 0°$ and 180° in Mode 1 or Mode 4, and Figs. 7(c) or 7(l) shows the 0° or 90° tilted linear polarization pattern in Mode 1 or Mode 4, respectively. Similarly, Figs. 7(d)–(e) or 7(g)–(h) show the electric field distributions when the $\phi = 0°$ and 180° at $\beta = 180°$ or 0° in Mode 2 or Mode 3, and Figs. 7(f) or 7(i) shows the 135° or 45° tilted linear polarization pattern in Mode 2 or Mode 3, respectively. The proposed array generates a horizontal polarization whose vector rotates every 45° throughout the four modes of the feeding network.

C. PARAMETRIC STUDY OF THE PROPOSED ARRAY

The proposed array with the proposed beamforming network operate from 5.03 GHz to 5.15 GHz which was the allocated

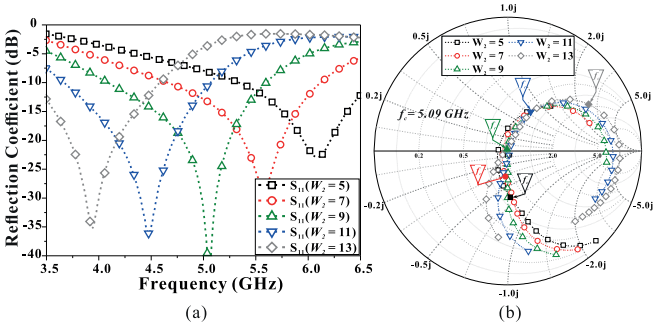

FIGURE 8. Simulated results of the proposed array with regard to the Mode 1: (a) simulated results of different antenna widths (W_2) on S_{11}, (b) simulated results of the W_2 on the Smith chart.

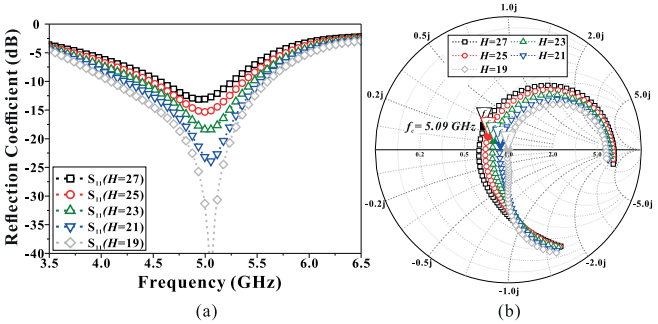

FIGURE 9. Simulated results of the proposed array with regard to the Mode 1: (a) simulated results of different antenna heights (H) on S_{11}, (b) simulated results of the H on the Smith chart.

UAV communication frequency in world radio communication conference-12 (WRC-12). The proposed array is simulated and optimized using a commercial full wave electromagnetic simulation tool (CST Microwave Studio 2019). Figs. 8–10 show the variation of S_{11}(reflection coefficient) at P1 (input port) and the impedance variation on Smith chart when the important parameter value of the proposed array is changed. Fig. 8(a) shows the simulated results for the reflection coefficients in Mode 1 at different antenna widths (W_2) ranging from 5 to 13 mm. When the W_2 is 5 mm, the 10-dB impedance bandwidth is approximately 15.7% (5.3 to 6.2 GHz), and when W_2 is 13 mm, the 10-dB impedance bandwidth is approximately 32.9% (3.3 to 4.6 GHz). Therefore, the operating frequency bandwidth is broadened when the W_2 increases. In addition, the resonant frequency of the proposed array shifts to a lower frequency band when the W_2 increases. The distance between the antennas represents by doubling the D. In Fig. 8(b), as the W_2 increases, the equivalent series inductance increases, and the resonance frequency of the array shifts to the lower frequency band. The proposed array has the good impedance matching at 5.1 GHz when the $W_2 = 9$ mm. Fig. 9(a) shows the simulated results for the reflection coefficients in Mode 1 at different heights (H) ranging from 19 to 27 mm. When the H is 19 mm, the reflection coefficient is approximately -34.9 dB at 5.1 GHz, and when the H is 27 mm, the reflection coefficient is approximately -12.4 dB at 5.1 GHz.

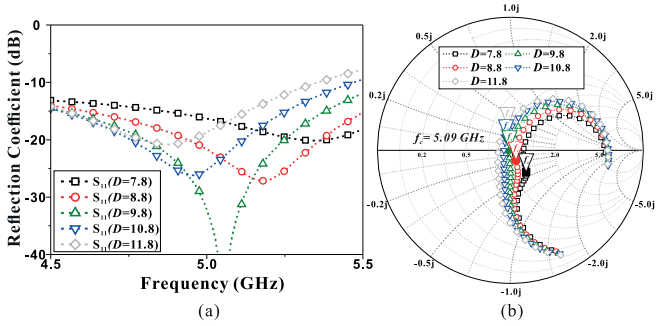

FIGURE 10. Simulated results of the proposed array with regard to the Mode 1: (a) simulated results of different antenna distances (D) on S_{11}, (b) simulated results of the D on the Smith chart.

Therefore, the reflection coefficient is improved when H decreases. It is depicted on the Smith chart in Fig. 9(b). In Fig. 9(b), as the H decreases, the equivalent parallel capacitance between the antenna array and the reflector increases. Fig. 10(a) shows the simulated results for the reflection coefficients in Mode 1 at different distances (D) ranging from 7.8 to 11.8 mm. When the $D = 7.8$ mm, the maximum reflection coefficient is approximately -20.1 dB at 5.3 GHz, and when $D = 27$ mm, the maximum reflection coefficient is approximately -20.8 dB at 4.9 GHz. The resonant frequency of the antenna shifts to a lower frequency band when the D increases. The reason why the resonant frequency shifts is depicted on the Smith chart in Fig. 10(b). The resonance frequency is shifted to the lower frequency band as the equivalent series capacitance decreases when the D increases. When the $D = 9.8$ mm, the reflection coefficient is approximately -45.3 dB at 5.1 GHz. When the $H = 19$ mm as the distance between the antenna radiator and the reflector, the impedance is matched and the gain of the array is maximized. The last important parameter value is antenna distance (D) which represents the distance from the radiator center to one antenna element.

IV. EXPERIMENTAL VERIFICATIONS

To verify the proposed design, the fully functional prototype of the proposed array in Fig. 11(a) was fabricated. All substrates of the proposed array use TACONIC RF-60 ($\varepsilon_r = 6.15$, and $\tan\delta = 0.002$). Their thicknesses are 0.64 mm and the copper thicknesses are 18 μm. In Fig. 11(b), the SP4T and SP3T switches for selecting and making four linear polarization modes were SKY13322-375LF (absolute maximum input power = 33 dBm, 1 dB input compression point = 30 dBm) and SKY13408-465LF (absolute maximum input power = 40 dBm, 1 dB input compression point = 34 dBm) made by Skyworks, respectively. The 90° hybrid coupler is CMX55Q03 by RN2 Technologies. Figs. 11(c)–(d) describe that the Wilkinson power divider of the proposed reconfigurable feeding network is PDW06398 by Knowles Dielectric Labs, and the tapered balun is used for the antenna feeding. Fig. 11(e) depicts the UAV with the mounted proposed

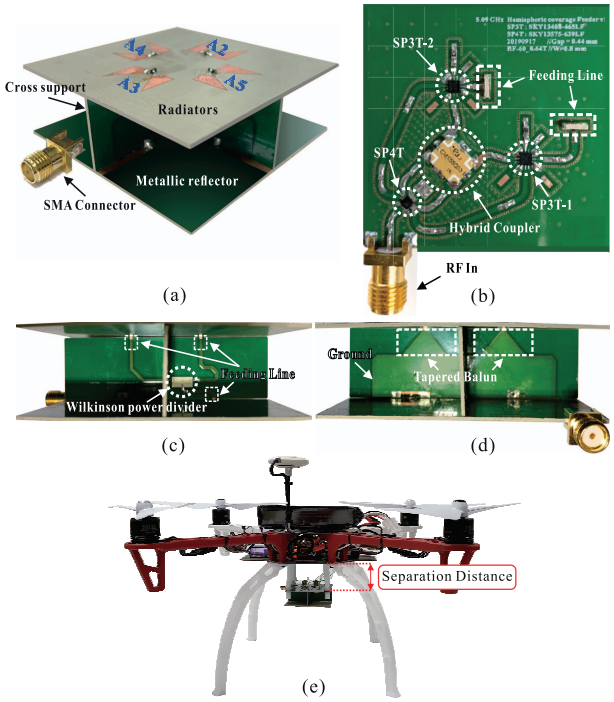

FIGURE 11. Photographs of the array prototype: (a) a perspective view, (b) a bottom view, (c)–(d) side views, (e) the UAV with the mounted proposed array.

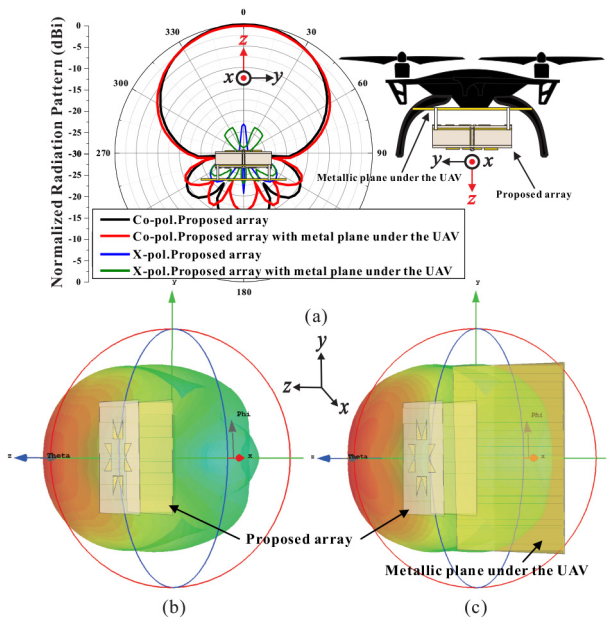

FIGURE 12. Simulated 2-D and 3-D radiation patterns: (a) simulated 2-D radiation patterns of the proposed array with regard to the UAV metallic effect at 5.1 GHz on the *yz* plane in total modes, (b)–(c) 3-D radiation patterns of the proposed array without or with the metal plane for the UAV in total modes, respectively.

array. The proposed array is separated with the metallic plane (ground plane of 120 × 180 mm^2) of the UAV by approximately 40 mm.

Fig. 12 shows the simulated 2-D and 3-D radiation patterns. To analyze the radiation pattern of the UAV-mounted antenna, the metallic plane (ground plane) was used to

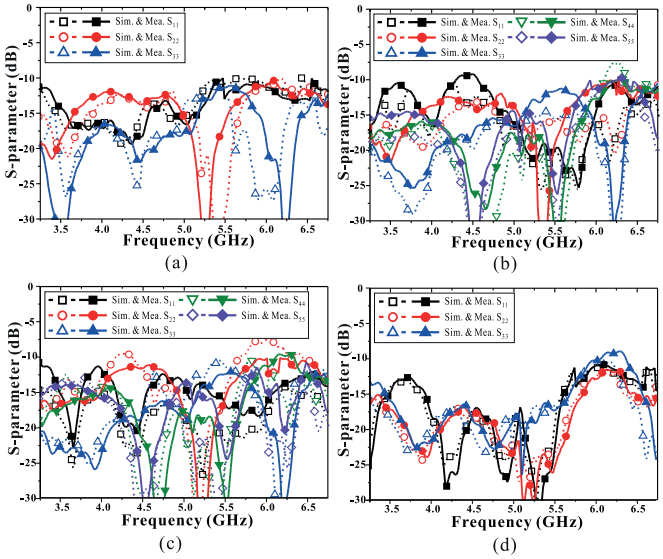

FIGURE 13. Simulated and measured reflection coefficients of the proposed array with regard to different modes: (a) Mode 1, (b) Mode 2, (c) Mode 3, and (d) Mode 4. The S_{11}, S_{22}, S_{33}, S_{44}, and S_{55} are the reflection coefficients of the RF input port (P1) and the antenna input ports (A1, A2, A3, and A4), respectively.

simulate the influence of the UAV on the proposed array according to previous studies [28]–[30]. Fig. 12(a) describes the simulated 2-D radiation patterns of the proposed array with regard to the UAV metallic effect at 5.1 GHz on the *yz* plane in total modes. Figs. 12(b)–(c) show the 3-D radiation patterns of the proposed array without or with the metal plane for the UAV, respectively. Their simulated results show that there is little influence on the beam pattern by the metallic effect in the proposed array. Therefore, the UAV does not affect the radiation characteristics of the proposed array. This is because there is an adequate separation distance between the UAV and the proposed array, and the metallic reflector of the array reduces back radiation.

Fig. 13 and Fig. 14 show the simulated and measured results (reflection coefficients, transmission coefficients, and phase difference) of the proposed array with regard to different modes (Mode 1 - Mode 4). The measured results have a good agreement with the simulated results. The S_{11}, S_{22}, S_{33}, S_{44}, and S_{55} are the reflection coefficients of the RF input port (P1) and the antenna input ports (A1, A2, A3, and A4), respectively. The S_{21}, S_{31}, S_{41}, and S_{51} are the transmission coefficients between the RF input port and the antenna input ports, respectively. In Mode 1, the measured results of the proposed reconfigurable feeding network are shown in Fig. 13(a) and Fig. 14(a). The measured maximum reflection coefficient and phase differences at 5.1 GHz are approximately −15.9 dB and −0.6°, respectively. The transmission coefficient between the RF input port and the antenna ports in the proposed reconfigurable feeding network is approximately −5.4 dB. It includes an ideal power dividing loss of 3 dB, the SP4T switch loss of 2 dB and the SP3T switch loss of 1 dB, respectively. In Fig. 13(b) and Fig. 14(b)

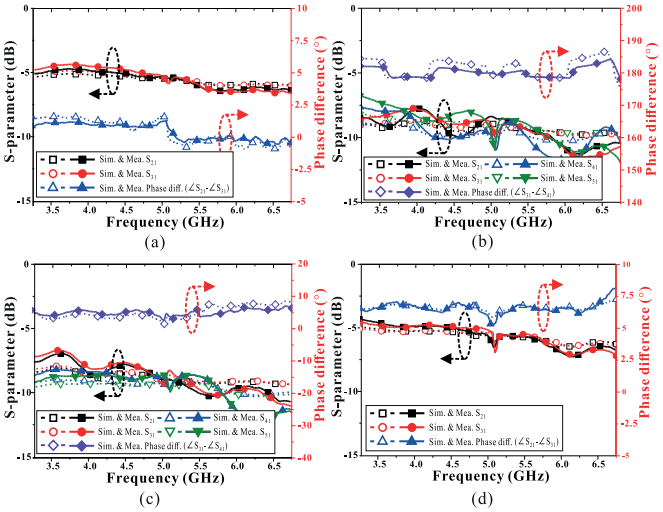

FIGURE 14. Simulated and measured results (transmission coefficients and phase difference) of the proposed array with regard to different modes: (a) Mode 1, (b) Mode 2, (c) Mode 3, and (d) Mode 4. The S_{21}, S_{31}, S_{41}, and S_{51} are the transmission coefficients between the RF input port and the antenna ports, respectively.

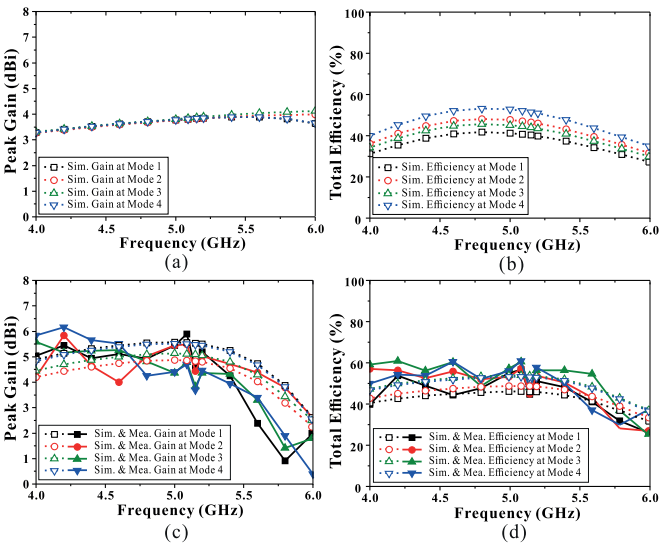

FIGURE 15. Simulated and measured peak gains and total efficiencies of the proposed array with/without a reflector: (a)–(b) simulated results without a reflector, (c)–(d) simulated and measured results with a reflector, respectively.

the maximum reflection coefficient and phase difference measured at 5.1 GHz in Mode 2 are approximately −15.3 dB and −166.8°, respectively. In addition, the minimum reflection coefficient and phase difference within the operating frequency band are approximately −20.7 dB and −178.5°, respectively. The transmission coefficient is approximately −9.6 dB including one 90° hybrid coupler loss of 3 dB, one Wilkinson power divider loss of 3 dB and two switches loss of 3 dB. The simulated and measured results of the proposed feeding network in Mode 3 are shown in Fig. 13(c) and Fig. 14(c). The reflection coefficient and phase difference measured at 5.1 GHz are approximately −14.8 dB and −0.57°, respectively. The transmission coefficient is approximately −9.2 dB. Fig. 13(d) and Fig. 14(d) show

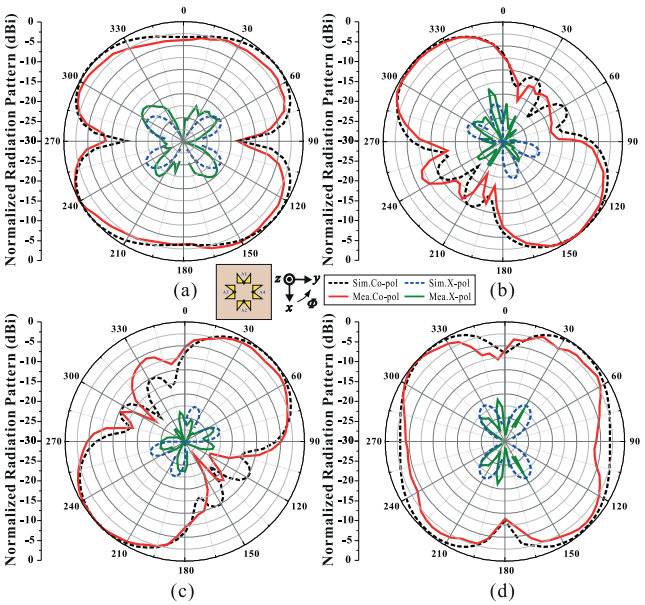

FIGURE 16. Simulated and measured radiation patterns of the proposed array at 5.1 GHz on the *xy* plane in different modes: (a) Mode 1, (b) Mode 2, (c) Mode 3, (d) Mode 4.

the simulated and measured results of the proposed feeding network in Mode 4. The measured maximum reflection coefficient and phase difference at 5.1 GHz are approximately −17.7 dB and −1.8°, respectively. The transmission coefficient is approximately −6.5 dB. It is included dividing power loss of 3 dB and two switches loss of 3 dB, respectively. In Fig. 6(a), the proposed array has a metallic reflector in the bottom substrate containing the reconfigurable feeding network. The reflector has an important role of reducing the back radiation and enhancing the radiation gain. Figs. 15(a)–(b) show the simulated peak gains and total efficiencies of the proposed array without a reflector at the operating modes. The simulated peak gain and total efficiency of the proposed array without a reflector are approximately 3.9 dBi and 52%, respectively. On the other hand, Fig. 15(c)–(d) show that the simulated peak gain and efficiency of the proposed array with a reflector at 5.1 GHz are approximately 5.6 dBi and 54.4%, respectively. From the reflector effect, the peak gain and total efficiency of the proposed array are improved by approximately 1.7 dBi and 2.4%, respectively. Also, Figs. 15(c)–(d) show the measured peak gain and total efficiency of the proposed array with a reflector. The measured peak gain and total efficiency of the proposed array are approximately 5.9 dBi and 62%, respectively. From Figs. 15(c)–(d), it can be seen that the measured results are almost similar to the simulated results.

Figs. 16–19 show the simulated and measured radiation pattern of the proposed array. Co-pol and X-pol mean co-polarization and cross-polarization, respectively, and their definitions are introduced in [31]. According to [32], the main beam directions in different modes (i.e., the main

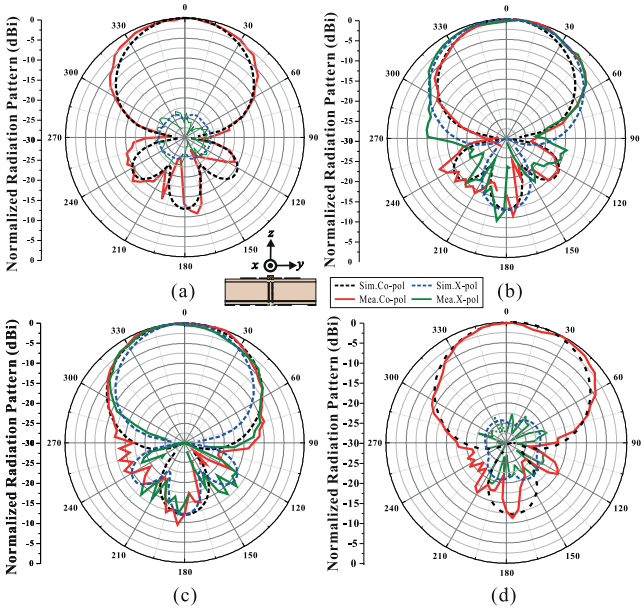

FIGURE 17. Simulated and measured radiation patterns of the proposed array at 5.1 GHz on the *yz* plane in different modes: (a) Mode 1, (b) Mode 2, (c) Mode 3, (d) Mode 4.

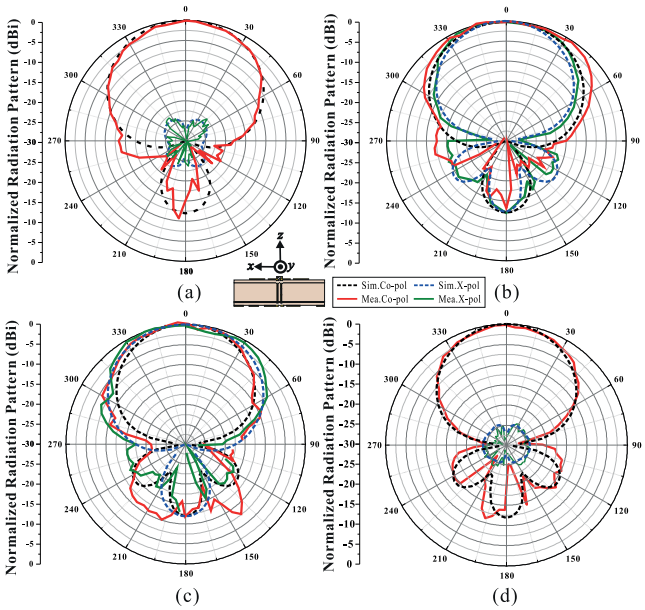

FIGURE 18. Simulated and measured radiation patterns of the proposed array at 5.1 GHz on the *xz* plane in different modes: (a) Mode 1, (b) Mode 2, (c) Mode 3, (d) Mode 4.

beam direction of Co-pol) are ϕ angles of 0°, 135°, 45° and 90° respectively. The X-pol formed in the direction crossing Co-pol is included in Figs. 16–19. In Figs. 16(a)–(d), the simulated and measured radiation patterns of the proposed array at 5.1 GHz on the *xy* plane in different modes are shown. The measured results have a good agreement with the simulated results. The half-power beamwidths (HPBWs) in different mode (Mode 1 – Mode 4) are approximately 240°, 99.6°, 99.6°, and 240°, respectively. Figs. 17(a)–(d) are the radiation patterns when $\phi = 90°$ (*yz* plane). In this

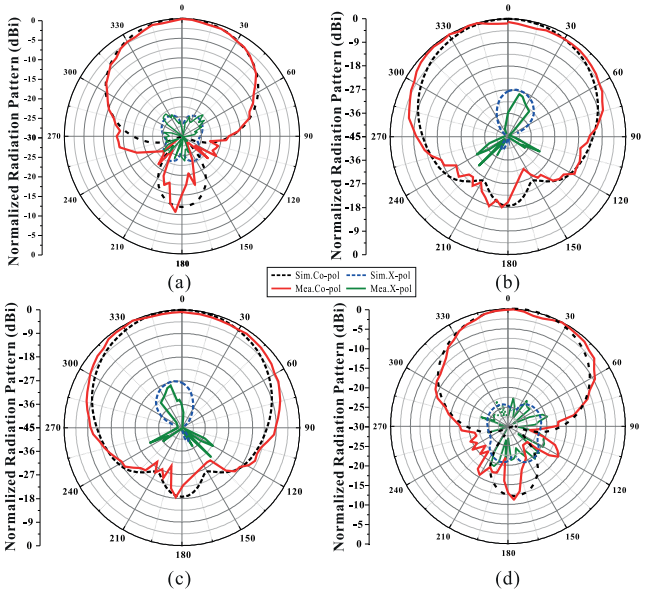

FIGURE 19. Simulated and measured radiation patterns at the main beam directions (0°, 135°, 45°, 90°) at 5.1 GHz: (a) Mode 1, (b) Mode 2, (c) Mode 3, (d) Mode 4.

case, the HPBWs in different modes (Mode 1 – Mode 4) are approximately 61.4°, 69.1°, 69.1°, and 77.4°, respectively. In Figs. 18(a)–(d), the HPBWs at $\phi = 0°$ (*zx* plane) are approximately 77.4°, 69.1°, 69.1°, and 61.4°, respectively. Co-pol and X-pol in Figs. 17(b)–(c) and Figs. 18(b)–(c) are almost identical at *yz*- and *zx*-planes because the main beam direction of mode 2 (mode 3) is 135° (45°). Figs. 19(a)–(d) show the radiation patterns at the main beam directions (0°, 45°, 90°, 135°) at 5.1 GHz in the different modes. In Fig. 19(a), the HPBW at $\phi = 0°$ is approximately 77.4°, and in Fig. 19(b), the HPBW at ϕ = 135° is approximately 98.6°. Fig. 19(c)–(d) describe the HPBWs at $\phi = 45°$ and $\phi = 90°$ are approximately 98.6° and 77.4°, respectively. Therefore, the HPBW at 5.1 GHz on the azimuth and elevation planes are approximately 240° and 99°, respectively. In Fig. 17 and Fig. 18, since the main beam directions of Mode 2 and Mode 3 are 135° and 45°, respectively, co-pol and cross-pol have the same radiation pattern when measured at $\phi = 0°$ and 90°.

Table 2 shows the comparison between previous works for UAV communications and the proposed array. Researches with elevation coverage have been conducted [11], [16]–[23]. Antennas that covering the azimuth plane were proposed ([11], [16]–[20]). These antennas have low-profile and small cross-sectional area (except [19] and [20]), but cannot cover the elevation plane. In order for the UAVs to communicate at different heights, the antenna for the UAV Communications must cover wide elevation angles. compared to other works ([21]–[23]), [1] and [13] have a small size and wide elevation angles, but have a low gain. The antennas proposed in [21]–[23] all have a uniform beam width (60°) in the elevation. In addition, it has a gain of 4.5 dBi (or 4.5 to 5 dBi). The proposed array has improved performances

with a wide beam coverage, wide bandwidth, high gain, and compact size.

V. CONCLUSION

We proposed a wideband printed half bow-tie antenna array with four linear polarizations for UAV communications in this article. For wide impedance band and compact size, the proposed array was applied to the printed half bow-tie antenna array. By controlling the amplitude and phase using three RF switches in the reconfigurable feeding network, the proposed array can be operated on four linear polarization modes for wide beam coverage. The proposed array achieves a wide beam elevation angle by placing each antenna element on a two-dimensional plane unlike the previously developed complex three-dimensional antennas ([11], [20]–[21]). The measured results show that the proposed array has a wide beam coverage and a wide bandwidth as well as a miniaturized size, a high gain, and a low-profile symmetrical structure for ease of installation and aerodynamic drag reduction in UAV. Therefore, the proposed array is competitive and suitable for several UAV applications.

REFERENCES

[1] J.-M. F. Gonzalez, P. Padilla, J. F. Valenzuela-Valdes, J.-L. Padilla, and M. Sierra-Perez, "An embedded lightweight folded printed quadrifilar helix antenna: UAV telemetry and remote control systems," *IEEE Antennas Propag. Mag.*, vol. 59, no. 3, pp. 69–76, Jun. 2017.

[2] Y. Chen and C.-F. Wang, "Electrically small UAV antenna design using characteristic modes," *IEEE Trans. Antennas Propag.*, vol. 62, no. 2, pp. 535–545, Feb. 2014.

[3] S. Hayat, E. Yanmaz, and R. Muzaffar, "Survey on unmanned aerial vehicle networks for civil applications: A communications viewpoint," *IEEE Commun. Surveys Tuts.*, vol. 18, no. 4, pp. 2624–2661, Apr. 2016.

[4] H. Shakhatreh *et al.*, "Unmanned aerial vehicles (UAVs): A survey on civil applications and key research challenges," *IEEE Access*, vol. 7, pp. 48572–48634, 2019.

[5] E. P. de Freitas, T. Heimfarth, A. Vinel, F. R. Wagner, C. E. Pereira, and T. Larsson, "Cooperation among wirelessly connected static and mobile sensor nodes for surveillance applications," *Sensors*, vol. 13, no. 10, pp. 12903–12928, Oct. 2013.

[6] Y. Zeng, R. Zhang, and T. J. Lim, "Wireless communications with unmanned aerial vehicles: Opportunities and challenges," *IEEE Commun. Mag.*, vol. 54, no. 5, pp. 35–42, May 2016.

[7] Y. Takahashi, Y. Kawamoto, H. Nishiyama, N. Kato, F. Ono, and R. Miura, "A TD-LTE-A based efficient radio access scheme for real-time data transmission over relay unmanned aerial vehicle networks," in *Proc. IEEE 86th Veh. Technol. Conf.*, 2017, pp. 1–5.

[8] I. Bekmezci, O. K. Sahingoz, and S. Temel, "Flying ad-hoc networks (FANETs): A survey," *Ad Hoc Netw.*, vol. 11, no. 3, pp. 1254–1270, May 2013.

[9] M. Mozaffari, W. Saad, M. Bennis, and M. Debbah, "Efficient deployment of multiple unmanned aerial vehicles for optimal wireless coverage," *IEEE Commun. Lett.*, vol. 20, no. 8, pp. 1647–1650, Aug. 2016.

[10] M. S. Sharawi, D. N. Aloi, and O. A. Rawashdeh, "Design and implementation of embedded printed antenna arrays in small UAV wing structures," *IEEE Trans. Antennas Propag.*, vol. 58, no. 8, pp. 2531–2538, Aug. 2010.

[11] Y.-H. Cui, P. Luo, Q. Gong, and R.-L. Li, "A compact tri-band horizontally polarized omnidirectional antenna for UAV applications," *IEEE Antennas Wireless Propag. Lett.*, vol. 18, no. 4, pp. 601–605, Apr. 2019.

[12] W. Lee *et al.*, "Dual-polarized hexaferrite antenna for unmanned aerial vehicle (UAV) applications," *IEEE Antennas Wireless Propag. Lett.*, vol. 12, pp. 765–768, Jul. 2013.

[13] Z.-Q. Liu, Y.-S. Zhang, Z. Qian, Z. P. Han, and W. Ni, "A novel broad beamwidth conformal antenna on unmanned aerial vehicle," *IEEE Antennas Wireless Propag. Lett.*, vol. 11, pp. 196–199, Feb. 2012.

[14] D.-G. Seo, J.-H. Kim, M. M. Tentzeris, and W.-S. Lee, "A quadruple-polarization reconfigurable feeding network for UAV RF sensing antenna," *IEEE Microw. Wireless Compon. Lett.*, vol. 29, no. 3, pp. 183–185, Mar. 2019.

[15] D. Wu, X. Chen, L. Yang, G. Fu, and X. Shi, "Compact and low-profile omnidirectional circularly polarized antenna with four coupling arcs for UAV applications," *IEEE Antennas Wireless Propag. Lett.*, vol. 16, pp. 2919–2922, Sep. 2017.

[16] L. Sun, B. Sun, J. Yuan, W. Tang, and H. Wu, "Low-profile, quasi-omnidirectional substrate integrated waveguide (SIW) multihorn antenna," *IEEE Antennas Wireless Propag. Lett.*, vol. 15, pp. 818–821, Sep. 2015.

[17] L. Sun, B.-H. Sun, Q. Sun, and W. Huang, "Miniaturized annular ring slot antenna for small/mini UAV applications," *Progr. Electromagn. Res.*, vol. 54, pp. 1–7, Oct. 2014.

[18] J. Tak and J. Choi, "A flush-mounted monopolar patch antenna for UAV applications," *Microw. Opt. Technol. Lett.*, vol. 59, no. 5, pp. 1202–1207, May 2017.

[19] D. Kang, J. Tak, and J. Choi, "Wideband low-profile planar square segmented loop antenna for UAV applications," *Electron. Lett.*, vol. 52, no. 22, pp. 1828–1830, Oct. 2016.

[20] S. Lee, G. Jeoung, and J. Choi, "Three-dimensional-printed tapered cavitybacked flush-mountable wideband antenna for UAV," *Microw. Opt. Technol. Lett.*, vol. 59, no. 12, pp. 2975–2981, Dec. 2017.

[21] N. Neveu *et al.*, "Miniature hexaferrite axial-mode helical antenna for unmanned aerial vehicle applications," *IEEE Trans. Magn.*, vol. 49, no. 7, pp. 4265–4268, Jul. 2013.

[22] M. S. Alam and A. Abbosh, "Planar pattern reconfigurable antenna with eight switchable beams for WiMax and WLAN applications," *IET Microw. Antennas Propag.*, vol. 10, no. 10, pp. 1030–1035, Jul. 2016.

[23] W. C. Zheng, L. Zhang, Q. X. Li, and Y. Leng, "Dual-band dual-polarized compact bowtie antenna array for anti-interference MIMO WLAN," *IEEE Trans. Antennas Propag.*, vol. 62, no. 1, pp. 237–246, Jan. 2014.

[24] D. G. Seo and W. S. Lee, "A multiply parasitic-coupled, three-dimensional antenna array with wide elevation angle for seamless UAV communications," *ACES J.*, vol. 35, no. 4, pp. 461–465, Apr. 2020.

[25] D. G. Seo, J. S. Park, G. K. Lee, and W. S. Lee, "Lightweight printed dipole antenna array with 3×2 beamforming network for wide UAV communication Coverage," *J. Elect. Eng. Technol.*, vol. 15, no. 4, pp. 1769–1773, 2020.

[26] C. A. Balanis, *Antenna Theory: Analysis and Design*, 3rd ed. New York, NY, USA: Wiley, 2005, pp. 284–289.

[27] R. G. Wu, M. G. Gao, J. L. Gai, and J. L. Bai, "Research on orthogonal half-wavelength dipole antenna," *Appl. Mech. Mater.*, vols. 20–23, pp. 801–807, Jan. 2010.

[28] J. L. Salazar, A. Umeyama, S. Duthoit, and C. Fulton, "UAS-based antenna pattern measurements and radar characterization," in *Proc. IEEE Conf. Antenna Meas. Appl. (CAMA)*, Sep. 2018, pp. 1–4.

[29] A. Y. Umeyama, J. L. Salazar-Cerreno, and C. J. Fulton, "UAV-based far-field antenna pattern measurement method for polarimetric weather radars: Simulation and error analysis," *IEEE Access*, vol. 8, pp. 191124–191137, 2020.

[30] A. Y. Umeyama, J. L. Salazar-Cerreno, and C. Fulton, "UAV-based antenna measurements for polarimetric weather radars: Probe analysis," *IEEE Access*, vol. 8, pp. 191862–191874, 2020.

[31] A. Ludwig, "The definition of cross-polarization," *IEEE Trans. Antennas Propag.*, vol. AP-21, no. 1, pp. 116–119, Jan. 1973.

[32] N. A. Aboserwal, J. L. Salazar, J. A. Ortiz, J. D. Díaz, C. Fulton, and R. D. Palmer, "Source current polarization impact on the cross-polarization definition of practical antenna elements: Theory and applications," *IEEE Trans. Antennas Propag.*, vol. 66, no. 9, pp. 4391–4406, Sep. 2018.

YE-YEONG JEONG (Student Member, IEEE) received the B.S. degree in electronic engineering from Gyeongsang National University, Jinju, South Korea, in 2019, where she is currently pursuing the M.S. degree.

Her current research interests include wide beam coverage antenna, beamforming antenna array and its feeding network for UAV communications, RF/microwave circuit and system, and RFID/IoT sensors.

WANG-SANG LEE (Senior Member, IEEE) received the B.S. degree from Soongsil University, Seoul, South Korea, in 2004, and the M.S. and Ph.D. degrees in electrical engineering from the Korea Advanced Institute of Science and Technology (KAIST), Daejeon, South Korea, in 2006 and 2013, respectively.

From 2006 to 2010, he was with the Electromagnetic Compatibility Technology Center, Digital Industry Division, Korea Testing Laboratory, Ansan, South Korea, where he was involved in the international standardization for radio frequency identification (RFID) and photovoltaic systems as well as electromagnetic interference (EMI)/EMC analysis, modeling, and measurements for information technology devices. In 2013, he joined the Korea Railroad Research Institute, Uiwang, South Korea, as a Senior Researcher, where he was involved in the position detection for high-speed railroad systems and microwave heating for low-vibration rapid tunnel excavation system. Since 2014, he has been an Associate Professor with the Department of Electronic Engineering, Gyeongsang National University, Jinju, South Korea. From 2018 to 2019, he was a Visiting Scholar with the ATHENA Group, Georgia Institute of Technology, Atlanta, GA, USA. His current research interests include near- and far-field wireless power and data communications systems, RF/microwave antenna, circuit, and system design, RFID/Internet of Things sensors, and EMI/EMC.

He was a recipient of the Best Paper Award at IEEE RFID in 2013, the Kim Choong-Ki Award—Electrical Engineering Top Research Achievement Award at the Department of Electrical Engineering, KAIST, in 2013, the Best Ph.D. Dissertation Award at the Department of Electrical Engineering, KAIST, in 2014, the Young Researcher Award at KIEES in 2017, and the Best Paper Awards at IEIE in 2018 and KICS in 2019. Dr. Lee is a Member of IEC/ISO JTC1/SC31, KIEES, IEIE, and KSR.